A 128 Gb/s PAM4 Silicon Microring Modulator With Integrated Thermo-Optic Resonance Tuning

Jie Sun, Ranjeet Kumar, Meer Sakib, Jeffrey B. Driscoll, Hasitha Jayatilleka, and Haisheng Rong

(Post-Deadline Paper)

***Abstract*—We report the first demonstration of a silicon photonic microring modulator with modulation data rate up to 128 Gb/s (64 Gbaud PAM4). The microring modulator exhibits an electro-optic phase efficiency of $V_\pi \cdot L = 0.52$ V·cm, an electro-optic bandwidth of 50 GHz, and a measured transmitter dispersion eye closure quaternary of 3.0 dB at this data rate. In addition, the resonant wavelength of the microring modulator can be tuned across a full free spectral range using an integrated heater with a thermo-optic phase efficiency of 19.5 mW/π-phase shift.**

***Index Terms*—Electro-optic modulators, integrated optoelectronics, optical interconnects, optical transmitters, photonics integrated circuits, silicon photonics.**

I. Introduction

SILICON photonics has emerged as a key enabling technology for current 100 Gb/s optical data center interconnects, and is considered an increasingly attractive solution as the industry moves towards 400 Gb/s to meet the ever-increasing data communication demand [1]. For 400 Gb/s data center optical interconnects, 4×100 Gb/s is a key IEEE 400G Ethernet standard, which necessitates the need to develop silicon photonic modulators capable of achieving >100 Gb/s data rate per wavelength. Such high data rates have been demonstrated in silicon Mach-Zehnder modulators [2], [3], which, however, require complex drivers such as traveling-wave or distributed electrodes due to their relatively large device length. In contrast, silicon microring modulators (MRM's) have some unique advantages such as small footprint, simpler driver architecture, and low power consumption. They are therefore particularly suitable for applications where space and power consumption are constrained and high bandwidth density is required [4]–[6]. Silicon MRM's have been extensively researched over the past years and data rates of up to 80 Gb/s have been demonstrated using four-level pulse-amplitude modulation (40 Gbaud PAM4) [7]–[12]. However, achieving beyond 100 Gb/s data rate has remained a major challenge for MRM's due to their intrinsic trade-off between bandwidth and modulation efficiency. In addition, to compensate for the wavelength mismatch between the MRM resonance and the laser due to both fabrication and temperature variations, a power-efficient resonance tuning element must be integrated into the MRM with the capability of tuning the ring resonance across a full free spectral range (FSR), which is also challenging given the already small footprint of the MRM. In this paper, we report the first demonstration of a silicon photonic MRM operating at 128 Gb/s (64 Gbaud PAM4). The MRM exhibits an electro-optic (EO) bandwidth of 50 GHz, phase efficiency of $V_\pi \cdot L = 0.52$ V·cm, a measured transmitter dispersion eye closure quaternary (TDECQ) of 3.0 dB at 128 Gb/s data rate, and an integrated silicon heater that can tune the ring resonance across more than one FSR with a thermo-optic tuning efficiency of 19.5 mW/π-phase shift.

Manuscript received August 7, 2018; revised August 30, 2018 and October 11, 2018; accepted October 12, 2018. Date of publication October 26, 2018; date of current version February 1, 2019. *(Corresponding author: Jie Sun.)*

The authors are with the Intel Corporation, Santa Clara, CA 95054-1549 USA (e-mail: jie1.sun@intel.com; ranjeet.kumar@intel.com; meer.nazmus.sakib@intel.com; jeffrey.b.driscoll@intel.com; hasitha.jayatilleka@intel.com; haisheng.rong@intel.com).

Color versions of one or more of the figures in this paper are available online at http://ieeexplore.ieee.org.

Digital Object Identifier 10.1109/JLT.2018.2878327

II. Microring Modulator Design

Fig. 1 shows a schematic of the designed silicon photonic MRM. The silicon waveguide was formed by a partial silicon etch followed by a full etch to create a ridge waveguide with 300-nm height and 400-nm width. The slab thickness was chosen to be 100 nm to better confine the mode and allow for small radii without introducing bending losses. The MRM presented here had a radius of 10 μm with an FSR of 6.6 nm. Fig. 1(b) illustrates a close-up view of the PN junction cross-section of the MRM. The PN junction, designed to operate in depletion mode, was formed in both vertical and horizontal directions in the center of the waveguide. Such a junction shape optimizes the EO phase efficiency by maximizing the optical mode overlap with the depletion region of the PN-junction. The width of the depletion region is given by

$$w = \sqrt{\frac{2\epsilon}{q} \cdot \frac{N_A + N_D}{N_A N_D}(V_0 - V)} \qquad (1)$$

where ϵ is the dielectric permittivity of silicon, q is the electron charge, $N_{A/D}$ is the *p*/*n*-type doping concentration, V_0 is the built-in voltage, and V is the bias voltage applied across the junction. Changing the bias voltage changes the depletion width, which in turn changes the refractive index of silicon and subsequently the resonance wavelength through the well-known plasma dispersion effect [13]. To the first order, the EO phase efficiency of silicon modulators is proportional to the square root of the doping concentration $\sqrt{N_{A/D}}$, as shown by (1).

0733-8724 © 2018 IEEE. Translations and content mining are permitted for academic research only. Personal use is also permitted, but republication/redistribution requires IEEE permission. See http://www.ieee.org/publications_standards/publications/rights/index.html for more information.

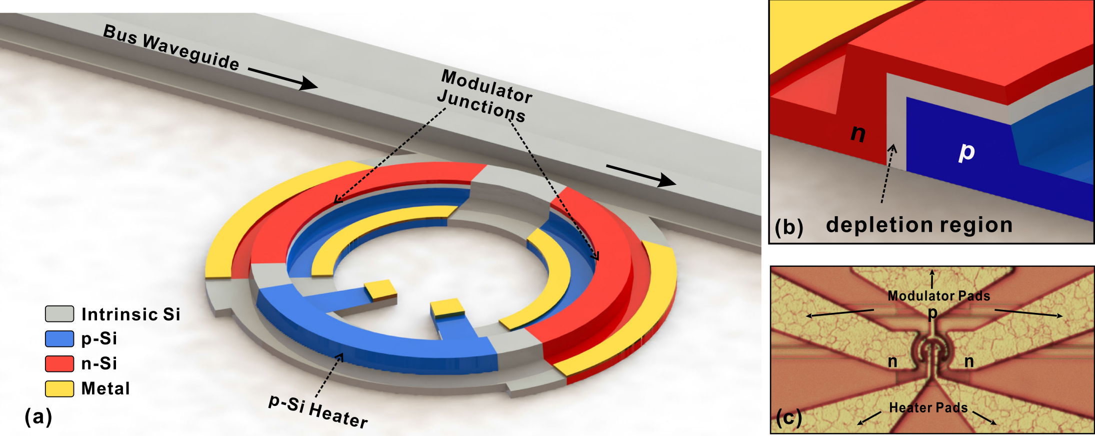

Fig. 1. (a) A schematic of the silicon photonic MRM including two segments of PN junctions and one segment of integrated silicon heater. (b) A close-up view of the depletion-mode PN junction which consists of a vertical part and a horizontal part to maximize the overlap with the optical mode. (c) An optical micrograph of the fabricated MRM.

Therefore, the EO phase efficiency can be increased by increasing the doping level. While increasing the doping level results in considerable insertion loss in silicon Mach-Zehnder modulators, it is much more tolerable for the MRM due to its small size. In addition, heavy doping also reduces the quality factor of the MRM and increases the photon-lifetime-limited optical bandwidth to enable high modulation bandwidth. It should be noted that the decreased quality factor also slows down the roll-off of the microring resonance and therefore reduces the optical modulation amplitude. As such, the ideal doping concentration should be at the level where the photon-lifetime-limited optical bandwidth and the resulting EO bandwidth is minimally sufficient to support the desired data rate. In this work, in order to support 64 Gbaud PAM4 modulation (128 Gb/s), the junction doping concentration was determined such that the MRM has a loaded quality factor Q of about 5000 which corresponds to a photon-lifetime-limited bandwidth of approximately 45 GHz. The electrical access to the junction from the metal contacts was through the silicon slab and the sidewall of the ring waveguide, as shown in Fig. 1(a). Multiple doping levels were employed to reduce the series resistance and to minimize the excess optical loss at the same time, which is essential to achieve a high electrical bandwidth in the presence of the relatively high capacitance due to the heavily doped junction. There are two segments of PN junctions in the MRM, as shown in Fig. 1(a), which in total occupy 67% of the ring circumference. Both segments were utilized in the following device characterization and modulation measurements.

The designed MRM was fabricated using Intel's silicon photonic process on a silicon-on-insulator (SOI) wafer. Fig. 1(c) shows an optical micrograph of the fabricated device, where the silicon MRM is buried underneath the metal electrodes. Fig. 2(a) shows the transmission spectra of the fabricated MRM at different reverse bias voltages. As expected, increasing the reverse bias voltage widens the depletion region, reduces the refractive index of the waveguide, and therefore red-shifts the resonance of the MRM. The measured extinction ratio was greater than 20 dB at the resonance wavelengths. This particular device shown in

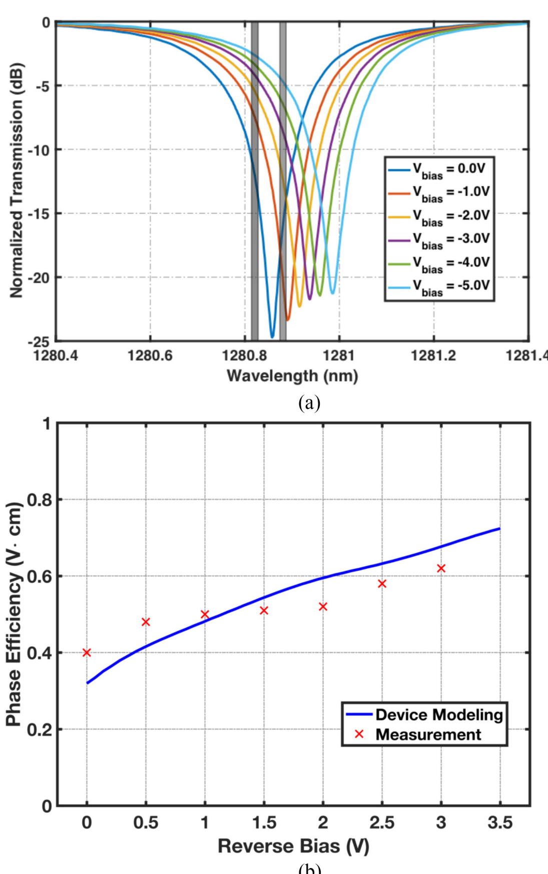

Fig. 2. (a) Measured transmission spectra of the MRM at different bias voltages. The shaded rectangles indicate the laser working wavelength used in the subsequent NRZ (left rectangle) and PAM4 (right rectangle) modulation measurements. (b) Measured (cross) and simulated (solid line) phase efficiency ($V_\pi \cdot L$) of the PN junction in the MRM.

Fig. 2 is slightly over-coupled where the coupling is a little larger than the round-trip cavity loss. As a result, the extinction ratio slightly decreases at higher reverse bias voltages due to the reduction in free carrier absorption (FCA) induced optical loss.

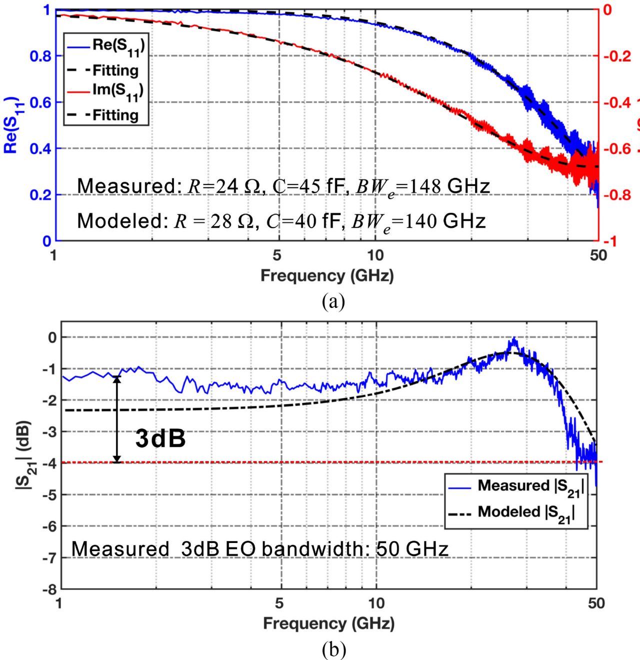

Fig. 3. (a) Measured (solid-line) electrical S_{11} parameter of the MRM at $V_{bias} = -2$ V and the fitting curves (dotted-line) to extract the device capacitance (45 fF) and resistance (24 Ω). (b) Measured (solid-line) EO response (S_{21}) of the MRM at $V_{bias} = -2$ V, showing an EO bandwidth of 50 GHz. The black dotted line shows the simulated EO S_{21} response.

The measured quality factor was 5500 and the corresponding photon-lifetime-limited optical bandwidth was approximately 42 GHz, slightly lower than the design. The EO phase efficiency, defined as the $V_\pi \cdot L$ value of the PN junction in the MRM, was shown in Fig. 2(b). The measured phase efficiency was 0.52 V·cm at a reverse bias voltage of 2 V and 0.4 V·cm at 0 V bias, agreeing with device simulations shown by the solid line in Fig. 2(b). The phase efficiency degrades at higher reverse bias voltages because the depletion width of the PN junction increases sublinearly with the bias voltage ($\propto \sqrt{V_0 - V}$), according to (1). This high EO phase efficiency originates from the engineered junction shape and location that maximally overlaps with the optical mode, and from the optimized doping concentration.

The frequency response of the fabricated MRM was measured using a vector network analyzer (VNA). As shown in Fig. 3(a), the electrical S_{11} response was measured at a reverse bias of 2 V and fit to a simple series RC equivalent circuit. The responses of cables and the probe were de-embedded through standard VNA calibrations. The extracted resistance and capacitance from the two-segment PN junction were 24 Ω and 45 fF, respectively. The resulting RC-limited electrical bandwidth was 148 GHz, which agrees well with simulations. Fig. 3(b) shows the measured electro-optic S_{21} response at the same reverse bias voltage of 2 V, indicating a combined EO bandwidth of 50 GHz. The dotted line in Fig. 3(b) shows the simulated S_{21} EO response which agrees well with the measurement. Note that the optical peaking shown in Fig. 3(b) around 30 GHz due to the intrinsic time dynamics in MRM's [14] extends the EO bandwidth to 50 GHz, beyond the 42-GHz photon-lifetime-limited bandwidth, making the MRM suitable to support 64 Gbaud PAM4 modulation (128 Gb/s).

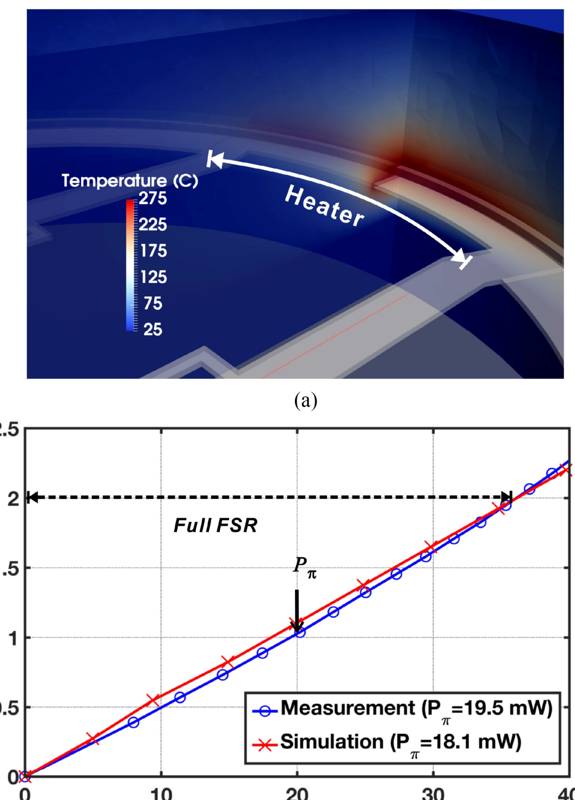

Fig. 4. (a) Simulated temperature distribution inside the microring modulator cavity to achieve π-phase shift using the integrated silicon waveguide heater. The heat concentrates around the core of the silicon waveguide to provide efficient thermo-optic tuning. (b) Measured and simulated thermo-optic phase shift at different heating power. Full-FSR tuning was achieved with a thermo-optic phase efficiency of $P_\pi = 19.5$ mW.

In addition to the modulator PN junction, a 10-μm long integrated heater was also formed as part of the MRM by doping the silicon waveguide, as shown in Fig. 1(a). Direct heating the silicon waveguide provides the best thermo-optic phase efficiency since it minimizes the heating volume and best overlaps with the optical mode [15], as shown in the 3D thermal simulation in Fig. 4(a) where the heat concentrates in the core of the silicon waveguide. In addition, the slab width in the heater region was also narrowed in order to further increase the thermal efficiency. Using the integrated heater, the resonance of the MRM can be tuned across more than one FSR, as shown in Fig. 4(b), and is sufficient to compensate for any wavelength mismatch with the laser due to both fabrication and temperature variations. The measured thermo-optic phase efficiency was $P_\pi = 19.5$ mW, in line with the 3D thermal simulation which predicted $P_\pi = 18.1$ mW.

III. High Speed Characterization

The fabricated MRM was driven by an arbitrary waveform generator (AWG), followed by a linear RF amplifier, a bias tee,

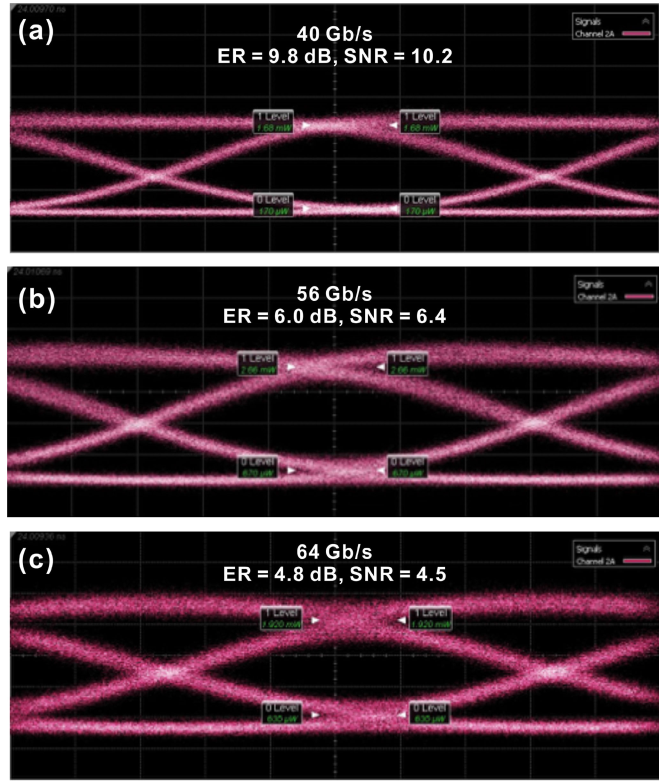

Fig. 5. Measured NRZ-OOK modulation eye diagrams of the MRM at data rate of (a) 40 Gb/s, (b) 56 Gb/s, and (c) 64 Gb/s. Open eyes were observed at all data rates.

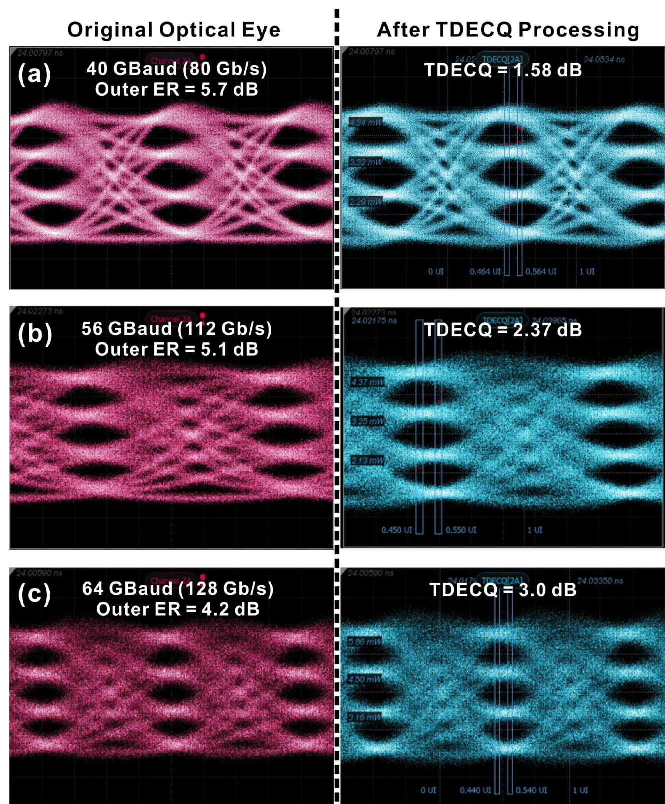

Fig. 6. Measured PAM4 modulation eye diagrams at symbol rate of 40 Gbaud (80 Gb/s), (b) 56 Gbaud (112 Gb/s), and (c) 64 Gbaud (128 Gb/s). For all data rates, the measured TDECQ was within the new IEEE 400G Ethernet standard which requires the TDECQ <3.4 dB at 53.125 Gbaud. Note that the left column shows the original eye diagrams as captured by the DCA, and the right column shows the post-processed eye diagrams by the TDECQ analysis software of the DCA using IEEE 802.3 bs specified settings.

and a 50-Ω terminated probe. The bandwidth limitation from the RF driver link, including the AWG frontend, RF amplifier, bias tee, and a long RF cable, was de-embedded based on the frequency response of the RF link which was measured by connecting the RF link to an 80 GHz electrical sampling module of a digital communication analyzer (DCA). This frequency response was then equalized up to 46 GHz through signal de-emphasis using the AWG (92 GSa/s) to provide high-quality electrical driving signals to the MRM. The optical input from a tunable laser was coupled into and out of the chip through vertical grating couplers. The modulated optical signal was amplified by a fiber optical amplifier and detected by the DCA with 65 GHz optical sampling module.

Figs. 5(a)–5(c) show the measured optical eye diagrams when the MRM was driven by non-return-to-zero on-off keying (NRZ-OOK) signals at data rates of 40 Gb/s, 56 Gb/s, and 64 Gb/s, respectively. The MRM was reverse biased at -2 V. The peak-to-peak RF swing was $V_{pp} = 2.5$ V at 56 Gb/s, corresponding to a calculated energy consumption of 70 fJ/bit [12]. The laser wavelength was tuned to 5∼6 dB down into the resonance at the corresponding DC bias. Open eyes were observed at all data rates. The modulation extinction ratio (ER) at the three data rates was measured to be 9.8 dB, 6.0 dB, and 4.8 dB, and the signal-to-noise ratio (SNR) was 10.2, 6.4, and 4.5, respectively. The 1-level insertion loss was 2.9 dB, 3.0 dB, and 3.2 dB at the three data rates.

The left column of Figs. 6(a)–6(c) show the measured optical eye diagrams when the MRM was driven by PAM4 signals at 40 Gbaud (80 Gb/s), 56 Gbaud (112 Gb/s), and 64 Gbaud (128 Gb/s), respectively. Here the MRM was biased at -4 V. The peak-to-peak RF swing was $V_{pp} = 2.4$ V at 56 Gbaud, corresponding to a calculated energy consumption of 18 fJ/bit [12]. The laser wavelength was tuned to about 6 dB down into the resonance at the corresponding DC bias. The outer ER, namely the modulation extinction ratio between the top level and the bottom level of the PAM4 eyes, was measured to be 5.7 dB, 5.1 dB, and 4.2 dB at 40 Gbaud, 56 Gbaud, and 64 Gbaud respectively. The top-level insertion loss was 3.8 dB, 4.0 dB, and 4.2 dB at these three baud rates. Again, open PAM4 eyes were observed at all data rates up to 128 Gb/s.

To further quantify the PAM4 modulation quality, we measured the TDECQ of the MRM transmitter. TDECQ represents the transmitter power penalty compared to an ideal virtual transmitter for PAM4 modulation, which is a practical method to quantitatively evaluate PAM4 modulation quality and has been adopted by the new IEEE standard for 200G and 400G Ethernet [16]. For example, the 400G BASE-DR4 standard requires the TDECQ penalty of <3.4 dB at symbol rate of 53.125 Gbaud (106.25 Gb/s). As shown in the right column of Figs. 6(a)–6(c), the measured TDECQ of the MRM was 1.58 dB, 2.37 dB, and 3.0 dB at symbol rate of 40 Gbaud (80 Gb/s), 56 Gbaud (112 Gb/s), and 64 Gbaud (128 Gb/s), respectively, all meeting the IEEE standard.

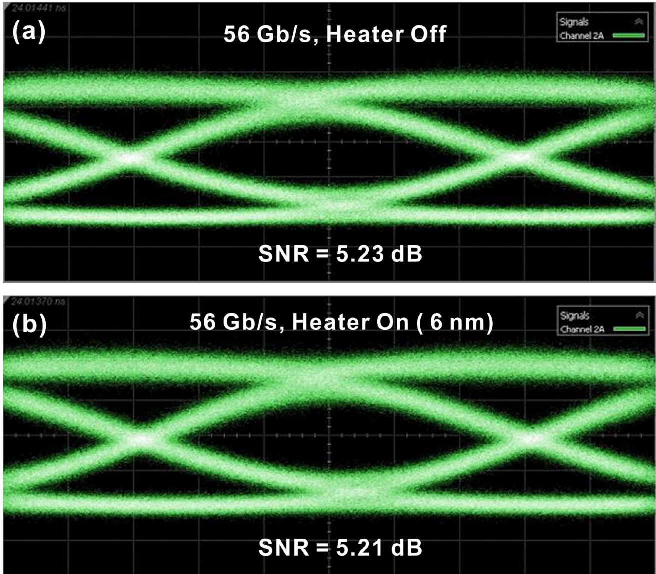

Fig. 7. Measured 56 Gb/s NRZ-OOK modulation eye diagrams of the MRM when (a) the integrated heater was off, and (b) the heater was on to tune the MRM resonance by 6 nm. No significant SNR degradation was observed.

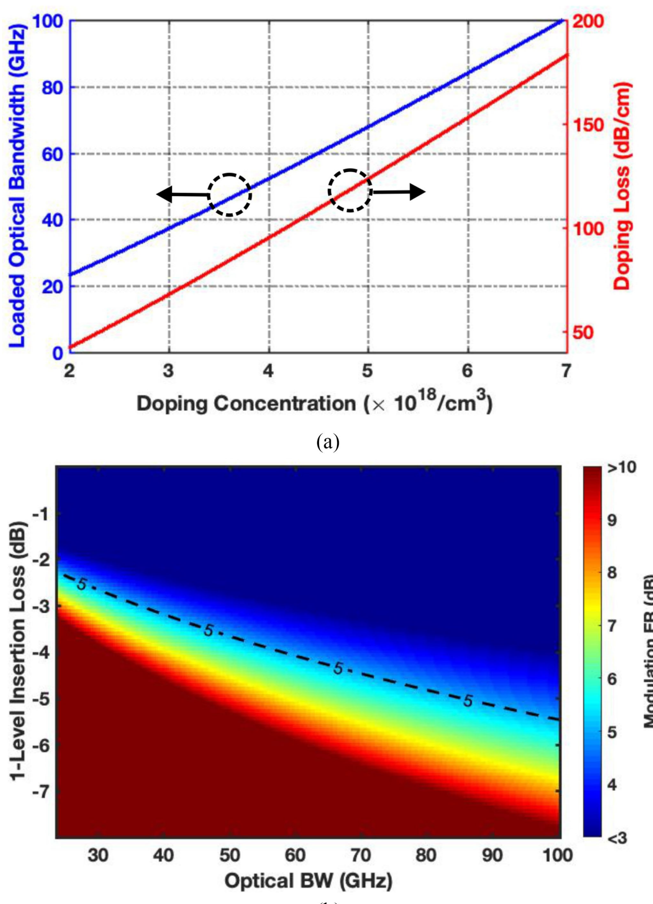

Fig. 8. (a) The calculated optical bandwidth and waveguide loss of the MRM at different doping concentrations. (b) Trade-off between modulation insertion loss and modulation extinction ratio of the MRM at different optical bandwidth with $V_{pp} = 2.5$ V in NRZ-OOK modulation. Note that a few approximations were made here to simplify the calculations. A uniform doping profile was assumed across the waveguide cross-section with equal p-type and n-type doping concentrations ($N_A = N_D$). The modulation phase efficiency was assumed to be proportional to $\sqrt{N_{A/D}}$ according to [10]. The MRM was working at critical coupling condition.

For practical applications, the silicon MRM's resonance wavelength must be tuned to match and track the laser wavelength that drifts with temperature during operation. Assuming that the laser and the MRM will experience similar ambient temperature changes, both the laser wavelength and the resonance wavelength of the MRM will change in the same direction with temperature. However, the rate of their wavelength changes will be different. We estimated that the wavelength walk-off between a typical InGaAsP based DFB laser and a silicon MRM will be less than 40 pm/° C, i.e., less than 4 nm when the chip temperature changes by 100°C which is more than required by most optical interconnect applications. As shown in Fig. 4(b), the integrated heater in the MRM was able to tune the resonance wavelength across a full FSR of 6.6 nm, sufficient to compensate for a wavelength mismatch between the laser and the MRM. We conducted an experiment to assess the impact of the ring resonance tuning using the integrated heater on MRM performance. We first set the laser to meet the MRM resonance at room temperature with the heater turned off, and we took an eye diagram, as shown in Fig. 7(a). Then we offset the laser wavelength by approximately 6 nm to mimic the worst-case wavelength drift in real-world operations, and turned on the heater to tune the MRM resonance by 6 nm to meet the laser wavelength, and repeated the eye diagram measurement, as shown in Fig. 7(b). In this experiment, NRZ-OOK modulation at 56 Gb/s was used with an RF swing of $V_{pp} = 1.8$ V. As shown in Fig. 7, when the MRM resonance was thermally tuned by 6 nm, no significant change in the eye SNR was observed.

IV. Future Work

Moving forward, several directions with potential can be further explored with the MRM. First, as shown by the electrical S_{11} measurements in Fig. 3, the RC-limited electrical bandwidth of the MRM is greater than 100 GHz. By further increasing its optical bandwidth using higher doping concentrations, an even higher EO bandwidth can be achieved to support data rates greater than 128 Gb/s. For instance, Fig. 8(a) calculates the optical bandwidth of the loaded, critically-coupled MRM at different junction doping concentrations [13], where an optical bandwidth as high as 100 GHz can be achieved at a reasonable doping level (7×10^{18} cm^{-3}). Although a higher doping concentration results in increased waveguide loss, it should be noted that in an MRM the waveguide loss does not directly correlate to the modulator insertion loss. In an MRM, the insertion loss is predominantly determined by the detuning of the working wavelength from the resonance wavelength. The detuning also affects the modulation extinction ratio. Fig. 8(b) shows the trade-off between the modulation extinction ratio and the insertion loss at different optical bandwidth (*i.e.* junction doping concentration) with an RF drive voltage of $V_{pp} = 2.5$ V in NRZ-OOK modulation.

Second, thanks to its compact size and low power consumption, a large number of MRMs can be integrated on the same

chip using wavelength division multiplexing to realize communication links with multi-terabit per second aggregate data rates.

V. Conclusion

We have demonstrated the first silicon microring modulator operating at 128 Gb/s (64 Gbaud PAM4) data rate. This was achieved by the MRM's high modulation phase efficiency of $V_\pi \cdot L = 0.52$ V·cm and simultaneously its high electro-optic bandwidth of 50 GHz. The transmitter penalty, TDECQ, of the PAM4 modulation at 56 Gbaud (112 Gb/s) and 64 Gbaud (128 Gb/s) was measured to be 2.37 dB and 3.0 dB respectively, well within the IEEE 400G Ethernet standard (802.3 bs for 53.125 Gbaud PAM4 transmitter). A silicon heater was also integrated as part of the MRM cavity that enabled a full-FSR thermo-optic wavelength tuning with a thermo-optic phase efficiency of 19.5 mW/π-phase shift, sufficient to compensate for the wavelength mismatch between the laser and MRM resonance. For a wavelength tuning range of 6 nm using the integrated heater, we observed no significant degradation of the SNR for 56 Gb/s NRZ-OOK modulation. This demonstration opens up the possibility of using compact, low power-consumption silicon microring modulators for the next generation 400G optical interconnects and beyond.

Acknowledgment

The authors would like to thank Y. Chetrit, L. Liao, D. Zhu, Y. Lin, H.-F. Liu, Y. Akulova, and B. Casper for fruitful technical discussions and our device fabrication partners in F11X, Intel Corporation, Rio Rancho, New Mexico, for their high-quality Si photonics processing support.

References

[1] T. Liljeberg, "Silicon photonics and the future of optical connectivity in the data center," in *Proc. IEEE Opt. Interconnects Conf.*, Jun. 2017, pp. 1–2.

[2] A. Samani *et al.*, "A low-voltage 35-GHz silicon photonic modulator-enabled 112-Gb/s transmission system," *IEEE Photon. J.*, vol. 7, no. 3, pp. 1–13, Jun. 2015.

[3] A. Samani *et al.*, "Experimental parametric study of 128 Gb/s PAM-4 transmission system using a multi-electrode silicon photonic Mach Zehnder modulator," *Opt. Express*, vol. 25, no. 12, pp. 13252–13262, Jun. 2017. [Online]. Available: http://www.opticsexpress.org/abstract.cfm?URI=oe-25-12-13252

[4] A. V. Krishnamoorthy *et al.*, "Computer systems based on silicon photonic interconnects," *Proc. IEEE*, vol. 97, no. 7, pp. 1337–1361, Jul. 2009.

[5] C. Sun *et al.*, "Single-chip microprocessor that communicates directly using light," *Nature*, vol. 528, pp. 534–583, Dec. 2015. [Online]. Available: http://dx.doi.org/10.1038/nature16454

[6] A. H. Atabaki *et al.*, "Integrating photonics with silicon nanoelectronics for the next generation of systems on a chip," *Nature*, vol. 556, no. 7701, pp. 349–354, 2018. [Online]. Available: https://doi.org/10.1038/s41586-018-0028-z

[7] Q. Xu, B. Schmidt, S. Pradhan, and M. Lipson, "Micrometre-scale silicon electro-optic modulator," *Nature*, vol. 435, pp. 325–327, May 2005. [Online]. Available: http://dx.doi.org/10.1038/nature03569

[8] G. Li *et al.*, "25 Gb/s 1V-driving CMOS ring modulator with integrated thermal tuning," *Opt. Express*, vol. 19, no. 21, pp. 20435–20443, Oct. 2011. [Online]. Available: http://www.opticsexpress.org/abstract.cfm?URI=oe-19-21-20435

[9] X. Xiao *et al.*, "60 Gbit/s silicon modulators with enhanced electro-optical efficiency," in *Proc. Opt. Fiber Commun. Conf. Expo. Nat. Fiber Optic Engineers Conf.*, Mar. 2013, pp. 1–3.

[10] E. Timurdogan, C. M. Sorace-Agaskar, J. Sun, E. Shah Hosseini, A. Biberman, and M. R. Watts, "An ultralow power athermal silicon modulator," *Nature Commun.*, vol. 5, Jun. 2014, Art. no. 4008. [Online]. Available: http://dx.doi.org/10.1038/ncomms5008

[11] M. Pantouvaki *et al.*, "Active components for 50 Gb/s NRZ-OOK optical interconnects in a silicon photonics platform," *J. Lightw. Technol.*, vol. 35, no. 4, pp. 631–638, Feb. 2017.

[12] R. Dubé-Demers, S. LaRochelle, and W. Shi, "Ultrafast pulse-amplitude modulation with a femtojoule silicon photonic modulator," *Optica*, vol. 3, no. 6, pp. 622–627, Jun. 2016. [Online]. Available: http://www.osapublishing.org/optica/abstract.cfm?URI=optica-3-6-622

[13] R. Soref and B. Bennett, "Electrooptical effects in silicon," *IEEE J. Quantum Electron.*, vol. 23, no. 1, pp. 123–129, Jan. 1987.

[14] J. Müller *et al.*, "Optical peaking enhancement in high-speed ring modulators," *Sci. Rep.*, vol. 4, 09 2014, Art. no. 6310. [Online]. Available: http://dx.doi.org/10.1038/srep06310

[15] M. R. Watts, J. Sun, C. DeRose, D. C. Trotter, R. W. Young, and G. N. Nielson, "Adiabatic thermo-optic Mach-Zehnder switch," *Opt. Lett.*, vol. 38, no. 5, pp. 733–735, Mar. 2013. [Online]. Available: http://ol.osa.org/abstract.cfm?URI=ol-38-5-733

[16] *IEEE Standard for Ethernet - Amendment 10: Media Access Control Parameters, Physical Layers, and Management Parameters for 200 Gb/s and 400 Gb/s Operation*, IEEE Std 802.3bs-2017 (Amendment to IEEE 802.3-2015 as amended by IEEE's 802.3bw-2015, 802.3by-2016, 802.3bq-2016, 802.3bp-2016, 802.3br-2016, 802.3bn-2016, 802.3bz-2016, 802.3bu-2016, 802.3bv-2017, and IEEE 802.3-2015/Cor1-2017), pp. 1–372, Dec. 2017.

Authors' biographies not available at the time of publication.